RSC Advances

ROYAL SOCIETY OF CHEMISTRY

www.rsc.org/advances

RSC Advances

ARTICLE

Improved Mechanical and Tribological Properties of Bismaleimide Composites by Surface-Functionalized Reduced Graphene Oxide and MoS_2 coated with Cyclotriphosphazene Polymer

Received 00th January 20xx,
Accepted 00th January 20xx

DOI: 10.1039/x0xx00000x
www.rsc.org/

Zhengyan Chen, Hongxia Yan*, Tianye Liu, Song Niu, Jiayi Ma

Surface-functionalized reduced graphene oxide and MoS_2 hybrid nanosheets (rGO/MoS_2) were obtained with coating poly-(cyclotriphosphazene-co-4,4'-diaminodiphenylmethane) polymer (PZD) by a one-pot noncovalent method. The PZD/rGO/MoS_2 hybrid nanoparticles were then chosen as fillers to improve the mechanical and tribological properties of bismaleimide (BMI) resin. The results showed that suitable addition of PZD/rGO/MoS_2 could greatly enhance not only mechanical and tribological properties but also thermal stability, such as the low friction coefficient of 0.06 and volume wear rate of 1.80×10^{-6} $mm^3/(N \cdot m)$ with 0.4 wt% PZD/rGO/MoS_2. This is mainly attributed to the unique layered structure of PZD/rGO/MoS_2 hybrid nanoparticles, enhanced toughness of the composites, good interfacial adhesion and compatibility between PZD/rGO/MoS_2 and BMI matrix, as well as the synergistic effect between nanosheets of rGO and MoS_2.

1 Introduction

Bismaleimide (BMI) is a leading class of thermosetting polyimides based on low molecules weight building blocks and terminated by reactive groups which undergo polymerization by thermal or catalytic means[1]. It is a material widely used in some of the most important areas, ranging from military programs such as the Air Force to electronic engineering[2, 3]. However, the cured resin is extremely brittle because of its high cross-link density, resulting in the poor mechanical property and friction performance. Therefore, it has been a hot point of research to modify and increase the friction performance of BMI resins.

As is well known, lubrication is one of the most effective approaches to reduce friction and wear in engineering[4, 5]. Two-dimensional graphene nanosheets and graphene-based materials have attracted significant attention in recent years due to their excellent material properties[6-9]. Owing to the unique structure of graphene, it has excellent thermal, electrical, and beneficial mechanical properties[10-12]. Especially, the graphene surface, formed by sp^2 bonded carbon atoms, is atomically flat and free of dangling bonds, which makes it an ideal starting template for other 2D materials[13]. In recent years, graphene or modified graphene have attracted increasing interest as fillers for polymer nanocomposites in the base-lubricant materials, such as poly(vinyl chloride), polyimide and BMI resin, to improve their friction and wear properties[14, 15]. Wang et al.[16] prepared multi-layer graphene filled poly(vinyl chloride) composites and discovered that the presence of multi-layer graphene could greatly decrease friction coefficient and wear rate of the composites. Min et al.[17] synthesized the graphene oxide/polyimide nanocomposites by situ polymerization and found that the composites exhibited better tribological properties under seawater-lubricated condition.

Recently, the versatility and success of graphene have also lead many researchers to investigate other two-dimensional nanomaterials, among which more attention has been paid to the typical layered transition metal dichalcogenides, in particular, MeX_2 (Me=Mo, W, Nb; X=S, Se, Te)[18, 19], which have an analogous structure to graphene. Especially, MoS_2 is the typical layered transition metal sulfide composed of three layers: a Mo layer sandwiched between S bilayers, and in which each layer consists of a covalently boned S-Mo-S hexagonal quasi-two-dimensional network, with weak van der Waals stacking between the layers[20-22]. MoS_2 is particularly important for solid lubrication or as an additive of "the king of lubrication" for a long time. It has been well known that nanosized MoS_2 usually has better tribological properties either in friction reduction or wear resistance than microsized and bulk MoS_2[23].

Since both MeX_2 and graphene have similar microstructure and morphology, heterolayered graphene/MeX_2 composites which maximize structural compatibility may synergize the MeX_2 nanosheets and graphene interaction, resulting in favorable outcomes greater than the sum of individual to components[24-27]. Therefore, significant efforts have been turned to fabricate graphene/MeX_2 composites. Yao et al.[28] prepared a sample of multilayer graphene and WS_2, which exhibited lower friction coefficient and wear rate; Li et al.[29] developed a facile and effective hydrothermal method to prepare $MoSe_2$ nano-flowers on reduced graphene oxide sheets, the composites as additives showed good friction and wear properties. However, to our knowledge, there is no literature so far investigating graphene/MoS_2 hybrid

[a] *Department of Applied Chemistry, School of Science, Northwestern Polytechnical University, Xi'an, Shaanxi, 710129, China. E-mail address: hongxiayan@nwpu.edu.cn; Fax: + 86 29 88431657*

nanoparticles as fillers in the application of friction resin matrix composites.

Polyphosphazenes are a versatile class of hybrid organic-inorganic materials possessing a backbone of alternating nitrogen and phosphorous atoms with remarkable properties and multiple applications[30, 31]. Surface functionalization of conventional fillers using polyphosphazenes has been carried out to modify the resins to improve the interfacial properties of composites[32]. In this study, a simple noncovalent side-wall functionalization of rGO/MoS_2 hybrids using poly-(cyclotriphosphazene-co-4,4'-diaminodiphenylmethane) (PZD) is reported. Subsequently, the PZD/rGO/MoS_2 hybrid nanoparticles were added as the solid lubricant and curing agent in BMI resin to fabricate PZD/rGO/MoS_2/BMI composites by a casting method. The as-fabricated composites exhibited excellent mechanical and tribological properties as well as thermal property.

2 Material and methods

2.1 Reagents and Materials

MoS_2 (99%, particle size <2 μm, #234842 Sigma-Aldrich) and NaCl (≥99.5%, #S7653 Sigma-Aldrich) were used as received. Natural graphite flakes (325 mesh) was obtained from Qingdao Hensen Graphite Co., Ltd. The graphene oxide (GO) nanosheets were produced from natural graphite flakes by a modified Hummers method[33]. Hexachlorotriphosphazene (HCCP), 4,4'-diaminodiphenylmethane (DDM) and triethylamine (TEA) were purchased from Aladdin Chemistry Co., Ltd. N-methylpyrrolidone (NMP), ethanol, tetrahydrofuran (THF), ammonia water and hydrazine hydrate were purchased from Tianjin Tianli Chemical Reagents Co. Ltd. The BMI was provided by Rongchang Ning research group at Northwestern Polytechnical University. Dially Bisphenol A (DBA) and 4,4'-bismaleimidodiphenylmethane (BDM) were purchased from Sigma-Aldrich. All reagents were of analytical grade and used as received without further purification.

2.2 Experimental section

2.2.1 Synthesis of rGO/MoS_2 Hybrids

Nanostructured MoS_2 was prepared from commercial bulk MoS_2 by the mechanochemical treatment method[34]. In a typical synthesis, 0.5 g MoS_2 and 5.0 g NaCl were added to the agate grinding bowl of planetary ball mill with the ball feed ratio of 1:7, grinding for 2 h with the rotation rate of 560 rpm. The obtained solid mixture was thoroughly washed for several times using deionized water to remove NaCl, and then dried under vacuum at 60 °C for 8 h to obtain the exfoliated MoS_2 nanosheets (exf-MoS_2). Then, 0.2 g exf-MoS_2 nanosheets and 0.4 g GO were dissolved in NMP and dispersed with ultrasound disintegration. Subsequently, the mixture was transferred to a 250 mL three-mouth flask holding a mechanical stirrer and was vigorously stirred at 25 °C for 2 days. Then two drops of concentrated hydrochloric acid were added to the reaction mixture, which was stirred in the sealed flask for 1 day at 80 °C. The black product was collected by centrifugation with deionized water and absolute ethanol for three times, respectively, freeze-dried for further reaction, and was recorded as GO/MoS_2.

Then the obtained GO/MoS_2 was dispersed in 180 mL distilled water through ultrasonication for 30 min. Subsequently, the mixture was transferred to a 250 mL three-mouth flask holding a mechanical stirrer and reflux-condenser, adding in 2.5 mL hydrazine hydrate and 7.5 mL ammonia water, and was heated to 98 °C for 6 h. After the reaction, the resulting product, abbreviated rGO/MoS_2, was filtered and washed with distilled water and ethanol for several times, and then dried under vacuum at 60 °C for 12 h.

2.2.2 Preparation of Poly-(cyclotriphosphazene-co-4,4'-diaminodiphenylmethane) Functionalized rGO/MoS_2 (PZD/rGO/MoS_2)

0.25 g rGO/MoS_2 and 100 mL THF were added into a beaker, followed by ultrasonication for 30 min. Then the mixture was transferred to a 250 mL round-bottomed flask holding a mechanical stirrer. Subsequently, 0.25 g HCCP, 0.4 g DDM and 3 mL TEA were added into the mixture solution. Then the reaction mixture was reacted at 50 °C for 4 h under ultrasonic irradiation (120 W). After the reaction, the mixture was filtered and washed with THF for several times to remove the uncoated PZD polymer. The resulting product was abbreviated PZD/rGO/MoS_2.

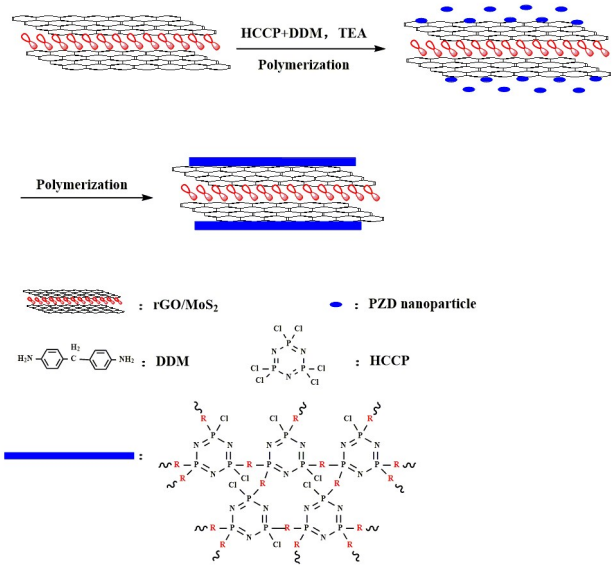

Fig. 1. The synthesis route of PZD functionalized rGO/MoS_2.

2.2.3 Preparation of PZD/rGO/MoS_2/BMI Composites

The PZD/rGO/MoS_2/BMI composites were prepared by a casting method. DBA and BDM with a mass ratio of 3:4 were heated to 140 °C in a glass beaker and kept at this temperature till totally melting. Then the suitable amount of rGO/MoS_2 was added into the melted BMI resin and stirred for about 30 min to disperse uniformly. Subsequently, the mixture was put into a pre-heated mold with release agent followed by degassing at 150 °C for about 1 h in a vacuum oven. After that, the mixture was cured following the schedule of 150 °C/2 h + 180 °C/2 h + 220 °C/4 h. A post curing process was 250 °C/4 h. Finally, the mold was cooled to room temperature and demolded to get the samples of PZD/rGO/MoS_2/BMI composites.

2.3 Characterizations

The X-ray diffraction (XRD) patterns of the samples were recorded on a Bruker D8 ADVANCE X-ray diffractometer with Cu Kα radiation (λ = 0.15405 nm). The 2ϑ angular regions between 5 ° and 85 ° were investigated with the scanning rate

of 0.02 ° s^{-1}. High resolution transmission electron microscopy (HRTEM) images were obtained with a JEOL JEM-200CX microscope operating at 200 kV. X-ray photo-electron spectroscopy (XPS, Thermal Scientific K-Alpha XPS spectrometer) was used to investigate the surface elemental composition of as-prepared samples. The analysis was performed under 1027 Torr vacuum with an AlKa X-ray source using a power of 200 W. Fourier Transform Infrared (FT-IR) spectra of the samples were recorded between 400 and 4000 cm^{-1} with a resolution of 2 cm^{-1} on a Nicolet FT-IR 5700 spectrometer (USA). Scanning electron micrographs (SEM) were performed on a HITACHIS-570 instrument. Raman spectra were recorded on a Renishaw Invia Plus Raman microscope using a 633 nm argon ion laser.

Impact strength was determined according to GB/T 2571-1995. Samples were cut into strips of (80 ± 0.2) × (10 ± 0.2) × (4 ± 0.2) mm^3 by a cutting machine. Flexural strength was measured according to GB/T 2570-1995. Samples were cut into strips of (80 ± 0.2) × (15 ± 0.2) × (4 ± 0.2) mm^3. The friction and wear tests were performed according to GB 3960-83 (Chinese Standard) on a test machine (M-200, load 196 N, rotate speed 200 rpm/min) under dry-sliding condition. The thermal gravimetrical analysis (TGA) tests were performed by using Perkin Elmer TGA-7 (USA) at a heating rate of 10 °C min^{-1} in an argon atmosphere from 50 to 800 °C.

3 Results and discussions

Fig. 2 shows the XRD patterns of bulk MoS_2, exf-MoS_2 and rGO/MoS_2 nanoparticles. All the sharp diffraction peaks of bulk MoS_2 can be attributed to hexagonal phase (JCPDS no. 37-1492). The strong (002) peak with a *d*-spacing of 0.62 nm signifies a well-stacked layered structure along the *c* axis[35]. After exfoliation, both restacked MoS_2 and rGO/MoS_2 show a much shorter (002) peak, indicating the decrease of crystallite size and the number of layers along the *c* axis[36]. It is noteworthy that the peaks of exf-MoS_2 and MoS_2/rGO hybrids shift much to the left, both appearing at 12.35°. According to the Bragg equation, the distance for *d* (002) of MoS_2 in the exf-MoS_2 and MoS_2/rGO hybrids were calculated to be 0.71 nm. Additionally, the rGO/MoS_2 nanoparticles still retain the position of the diffraction peaks of MoS_2, and the new diffraction peak of rGO at $2\vartheta \approx 24°$ can be detected. XRD results imply that the interlayer distance of MoS_2 is enlarged after exfoliation process, and the thickness of MoS_2 layers can be further reduced in rGO/MoS_2 hybrids due to the presence of rGO[37].

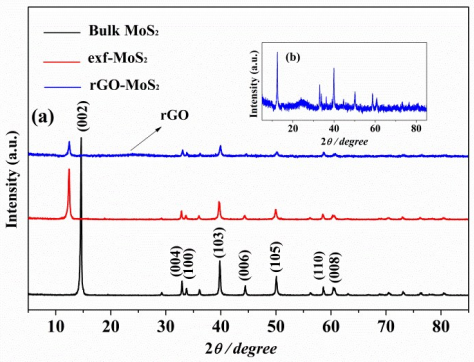

Fig. 2. (a) XRD patterns of bulk MoS_2, exf-MoS_2 and rGO/MoS_2 nanoparticles; (b) Magnified of rGO/MoS_2 nanoparticles.

In order to investigate the rGO/MoS_2 and PZD functionalization of rGO/MoS_2, XPS is employed. Fig. 3a provides the survey spectra of rGO/MoS_2 and PZD/rGO/MoS_2. In the XPS spectrum of rGO/MoS_2, three obvious peaks are observed at 286.0, 399.1 and 532.1 eV, corresponding to C 1s, N 1s and O 1s, respectively. Moreover, the binding energy of 229.2 and 162.8 eV, which is ascribed to Mo 3d and S 2p, respectively, are observed. These results mentioned above indicate that the rGO/MoS_2 is synthesized successfully. Compared to the rGO/MoS_2 spectrum, the XPS spectrum of PZD/rGO/MoS_2 shows significant amount of C 1s, which is ascribed to the coated 4,4'-diaminodiphenylmethane. In addition, new peaks at 129.7, 190.9 and 200.0 eV are corresponded to P 2p, P 2s and Cl 2p, respectively, which is attributed to the coated hexachlorotriphosphazene. The XPS spectrum of PZD/rGO/MoS_2 indicates that rGO/MoS_2 has been successfully functionalized with cyclotriphosphazene polymer containing phosphorus and nitrogen.

In detail, the C 1s XPS peak-fitting (Fig. 3b) shows four peaks at 284.5, 285.1, 285.9 and 287.5 eV, which are corresponded to sp^2-hybridized C=C double bond, sp^3-hybridized C-C single bond, carbon in C-O single bond and carbon in C=O double bond, respectively. There are two doublets of Mo-3d signals (Fig. 3c), the peaks of Mo 3d $_{5/2}$ and Mo 3d $_{3/2}$ with the binding energy of 229.2 and 232.4 eV, assigned to MoS_2, respectively. Meanwhile a small S 2s peak is located at a slightly lower binding energy of 226.4 eV (Fig. 3d). And the binding energy of 162.1 and 163.2 eV are corresponded to S 2p $_{3/2}$ and S 2p $_{1/2}$, respectively. Additionally, in Fig. 3e, the peaks attributed to the binding energy for P-Cl bond, P=N bond and P-N-C bond are observed at 132.98, 133.7 and 133.9 eV, respectively. The XPS spectra indicate that cyclotriphosphazene-co-4,4'-diaminodiphenylmethane polymer has been successfully coated onto the rGO/MoS_2 surface.

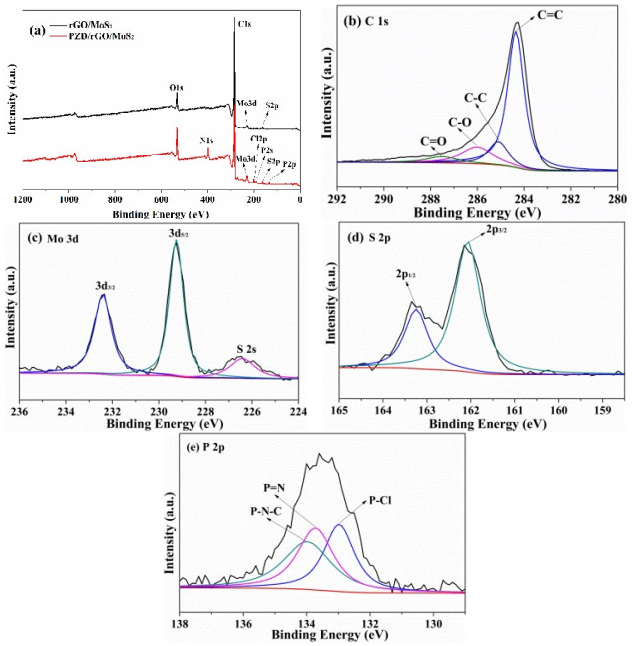

Fig. 3. XPS spectra of (a) rGO/MoS_2 and PZD/rGO/MoS_2; (b) C 1s; (c) Mo 3d; (d) S 2p; (e) P 2p of PZD/rGO/MoS_2.

FT-IR spectra of the as-prepared GO and PZD/rGO/MoS_2 nanoparticles are displayed in Fig. 4a. The characteristic peaks of GO appear at 3442, 1643 and 1040 cm^{-1}, which are ascribed to -OH, C=C and C-O vibrations, respectively. Furthermore, the peak of PZD/rGO/MoS_2 at 1643 cm^{-1} is corresponded to C=C vibrations, indicating the reduction of GO. By contrast, after coating cyclotriphosphazene polymer on the surface of rGO/MoS_2, the characteristic peaks at 1554 and 1380 cm^{-1}, which are attributed to the N-H bending vibration and the C-N stretching vibration of (Ph)-NH or (Ph)-NH_2, respectively, are observed[38]. The above signals are ascribed to DDM units. Meanwhile, the new peaks at 1173, 998, 900 and 610 cm^{-1} are attributed to asymmetric stretching vibration of the P=N and the P-N groups of the cyclophosphazene ring, to the P-N stretching vibration of new P-NH-(Ph) band, to the P-Cl absorption of the cyclophosphazene ring[39], respectively. These results also provide an evidence of successfully coating the cyclotriphosphazene polymer onto the surface of rGO/MoS_2.

Raman spectroscopy is applied to investigate the different microstructure of as-prepared GO, bulk MoS_2 and rGO/MoS_2. As shown in Fig. 4b, the two dominant peaks of pristine MoS_2 at 376 and 403 cm^{-1} are correspond to the E_{2g}^1 and A_{1g} modes of the hexagonal MoS_2, respectively[40]. The E_{2g}^1 mode accords with the in-layer displacement of Mo and S atoms, while the A_{1g} mode involves the out-layer symmetric displacement of S atoms along the *c* axis[41]. Besides the predominant MoS_2 peaks, two other Raman peaks at 1349 and 1596 cm^{-1}, which are attributed to D and G bands of rGO, can be detected in the rGO/MoS_2. The D band is ascribed to the disorder and defects of rGO, while the G band is attributed to the vibration of sp^2 carbon atoms. The relative intensity ratio I_D/I_G of GO is calculated 0.82, while the I_D/I_G in rGO/MoS_2 sample is calculated 1.19. The calculated I_D/I_G value of the rGO/MoS_2 nanoparticles has much increased compared to that of GO, which is attributed to the reduction of GO.

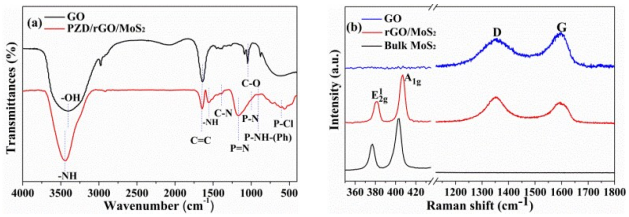

Fig. 4. (a) FT-IR spectra of as-prepared GO and PZD/rGO/MoS_2 nanoparticles; (b) Raman spectra of GO, bulk MoS_2 and rGO/MoS_2.

To better understand the microstructure and morphology of the rGO/MoS_2 and PZD/rGO/MoS_2 nanoparticles, we have performed TEM and HRTEM observations. It can be clearly seen that bulk MoS_2 (Fig. 5a) displays a perfect layered structure with the $d_{(002)}$ = 0.62 nm, which is well consistent with the XRD analysis for the hexagonal lattice of the MoS_2 phase. And after hybridization, as labeled in Fig. 5b and 5c, the rGO/MoS_2 hybrids are well fabricated in layer-by-layer, the exf-MoS_2 is well dispersed in the rGO, and the interlayer distance of rGO/MoS_2 hybrids is 0.71 nm, much larger than that of bulk MoS_2, which is consistent with XRD results. Compared to rGO/MoS_2 hybrids, some grey sheets on the surface of PZD/rGO/MoS_2 nanoparticles are observed in Fig. 5d, which can be attributed to the cyclotriphosphazene polymer coated onto the surface of rGO/MoS_2.

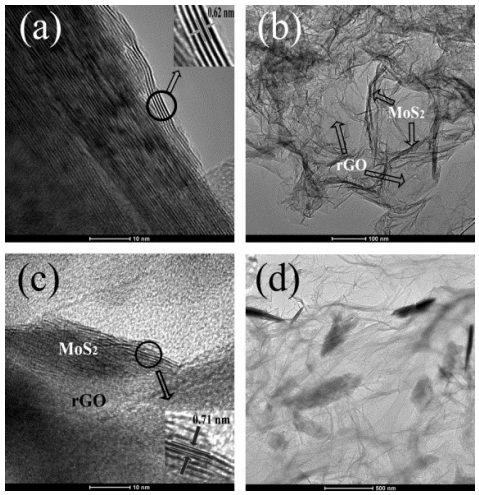

Fig. 5. TEM (b and d) and HRTEM (a and c), (a) bulk MoS_2; (b and c) rGO/MoS_2; (d) PZD/rGO/MoS_2 nanoparticles.

The dependency of the impact and flexural strength of the PZD/rGO/MoS_2/BMI composites on the content of the PZD/rGO/MoS_2 are shown in Fig. 6a and 6b. It can be clearly seen that appropriate amount of PZD/rGO/MoS_2 can properly improve the impact and flexural strength of the neat BMI resin. The impact and flexural strength increase continuously with the addition of PZD/rGO/MoS_2, which reach the maximum value of 15.98 kJ/m^2 and 179.32 Mpa with 0.6 wt% fillers, increased by 21.52% and 32.12% in comparison with those of the neat BMI resin (the impact and flexural strength of the neat BMI resin are 13.15 kJ/m^2 and 135.72 Mpa, respectively). This is mainly ascribed to the following reasons: (1) There is synergistic effect between the exf-MoS_2 and rGO, in addition, polyphosphazene is a kind of inorganic-organic polymer which can improve the compatibility with BMI resin, thus the unique structure of PZD/rGO/MoS_2 hybrids can increase dispersibility in BMI matrix, the improved dispersibility is the most important factor for effecting impact and flexural strength of the composites[42]; (2) -NH_2 groups in PZD/rGO/MoS_2 can react with carbon-carbon double band of the BMI resin, resulting in the improved interfacial bonding strength between PZD/rGO/MoS_2 and resin matrix[43]. However, when the content of fillers exceeds 0.6 wt%, the impact and flexural strength of the composites decrease and even lower than those of the neat BMI resin. This phenomenon can be explained that excessive PZD/rGO/MoS_2 hybrid nanoparticles can agglomerate in the matrix, therefore, the advantages of the PZD/rGO/MoS_2 are not fully realized[44].

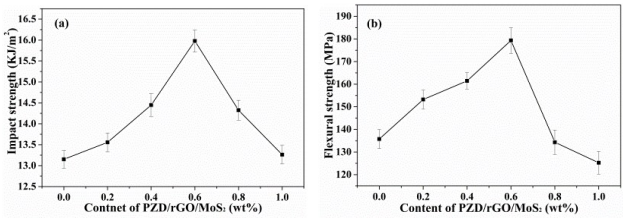

Fig. 6. Impact strength (a) and flexural strength (b) of composites with different contents of PZD/rGO/MoS_2.

In order to further confirm the effect of PZD/rGO/MoS_2 on the toughness of BMI resin, SEM images of the fracture surfaces of

the neat BMI resin and PZD/rGO/MoS_2/BMI composites taking from impact tests are shown in Fig. 7a and 7b. The fracture surface of the neat BMI resin is slick, exhibiting a typical brittle feature. While with the addition of 0.6 wt% PZD/rGO/MoS_2 into BMI resin, the fracture surface of composite is indented and exists large amount of ductile sunken areas, exhibiting a typical rough feature, which can absorb large amounts of energy of fracture and put off the micro-crack propagation. In addition, we can clearly see that there are no obvious aggregates on the fracture surface of the 0.6 wt% PZD/rGO/MoS_2/BMI composite, indicating that PZD/rGO/MoS_2 fillers are well compatible with the BMI resin matrix in proper amount. The features of the fracture surfaces of composites are well consistent with the improved impact strength of the composites.

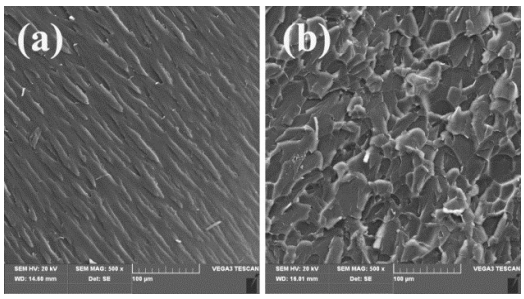

Fig. 7. SEM images of the fracture surfaces of (a) the neat BMI and (b) the composite with 0.6 wt% PZD/rGO/MoS_2.

Fig. 8a shows the change curves of friction coefficients of PZD/rGO/MoS_2/BMI composites as a function of PZD/rGO/MoS_2 content for steady-state sliding against the steel counterpart under dry conditions. It can be clearly seen that the neat BMI resin and the PZD/rGO/MoS_2/BMI composites all show high friction coefficient in the initial stage of friction, which is attributed to the fact that the real contact area between the rigid friction pairs and composites is relatively small, and the composites occurred the plastic deformation under shear stress during the dry-sliding friction, resulting in a rapid increase of the friction coefficient. Over time, the friction coefficient value of PZD/rGO/MoS_2/BMI composites decrease more sharply when the PZD/rGO/MoS_2 content is below 0.8 wt% (the fiction coefficient are as low as about 0.06), which is mainly attributed to the fact that the PZD/rGO/MoS_2/BMI composites are easier to be deformed under tangential stress than the neat BMI resin. On the other hand, a dense transfer film is formed on the surface of steel counterpart, providing the low-strength junction at the interface and making the friction mainly occur between the composites and the transfer film, resulting in lower friction coefficient of the composites. However, with further increasing of the concentration, the friction coefficient has a little increased but still much lower than that of the neat BMI resin, which is attributed to [45]the excessive PZD/rGO/MoS_2 agglomerates of BMI resin in the contact zone, which create more microcracks in the composites under high load, thus the load-carrying capability of the composites decreases, resulting in the deformation of the composite will increase during the wear process[46].

Fig. 8b shows volume wear rate of the composites with different PZD/rGO/MoS_2 contents. It can be observed that the volume wear rate decreases drastically with the addition of PZD/rGO/MoS_2, indicating that the composites have excellent wear resistance in its sliding against the steel counterpart. When the content of PZD/rGO/MoS_2 is 0.4 wt%, the volume wear rate of the composite reaches the lowest value by 1.80 × 10^{-6} mm^3/(N·m), decreasing as much as 89% compared to that of the BMI resin, of which volume wear rate is 16.35 × 10^{-6} mm^3/(N·m). While when the filler content is high enough (>0.6 wt%), the volume wear rate of composites increases but still much lower than that of the neat BMI resin, which can be ascribed to the agglomerates of the excessive PZD/rGO/MoS_2 nanoparticles in the matrix. In our work, the high wear resistance of the composites is mainly attributed to the enhanced toughness of the composites and high self-lubricant performance of the rGO and exf-MoS_2 hybrid nanosheets.

It can be seen from these results that the wear performance of PZD/rGO/MoS_2/BMI composites is related to their mechanical properties. When PZD/rGO/MoS_2 nanoparticles were added to the BMI resin matrix, the mechanical properties of composites increase and the wear properties decrease, while the tribological behavior of composites is dependent on not only the mechanical properties[45] but also the bonding strength between the PZD/rGO/MoS_2 and BMI resin as well as the transfer film on the surface of the steel counterpart. It was concluded that optimal mechanical properties does not coincide with optimal tribological properties[47].

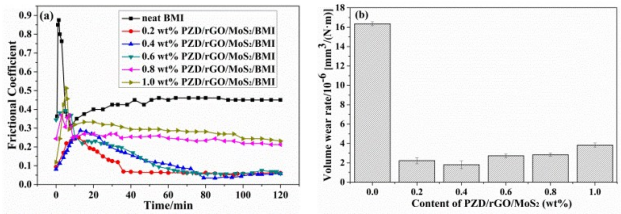

Fig. 8. Frictional coefficient (a) and volume wear rate (b) of the composites with different content PZD/rGO/MoS_2.

To investigate the worn surface morphology of the neat BMI resin and the composite with 0.4 wt% PZD/rGO/MoS_2, SEM micrographs are shown in Fig. 9a and 9b. We can clearly see that there are a plenty of deep scratches and a large-size wear debris left on the surface of the neat BMI resin (Fig. 9a), indicating a high wear rate and low wear resistance because of the brittle fracture of the neat BMI when sliding against the steel counterpart and its wear mechanism mainly follows abrasive wear mechanism. Compared to the worn surface of the neat BMI resin, the wear surface of the 0.4 wt% PZD/rGO/MoS_2/BMI composite is much milder and has few scales, exhibiting a high wear resistance of the composite and its wear mechanism primarily follows adhesive wear mechanism, which is mainly attributed to the enhanced toughness of composites and high self-lubricant performance of rGO and exf-MoS_2. This phenomenon can be explained in that good interfacial interaction and compatibility between PZD/rGO/MoS_2 nanoparticles and the BMI resin; furthermore, when the content of fillers is proper, composites can form a dense transfer film on the surface of the steel counterpart, which can decrease the friction and wear between composites and the steel counterpart, making the friction mainly occur between the composites and the transfer film. These explanations are in good agreement with the results described above that the 0.4 wt% PZD/rGO/MoS_2/BMI composite possesses the highest wear resistance.

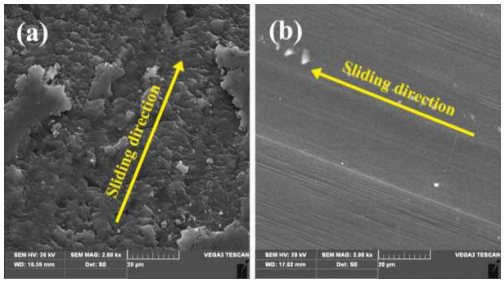

Fig. 9. SEM images of wear surface of (a) the neat BMI, (b) 0.4 wt% PZD/rGO/MoS_2/BMI composites.

The transfer films of the neat BMI resin and the composite with 0.4 wt% PZD/rGO/MoS_2 are shown in Fig. 10a and 10b, respectively. The SEM image of the steel counterpart surface of the neat BMI resin has a large amount of notches, indicating that the neat BMI composite cannot form the uniform and dense transfer film under dry sliding condition. On the other hand, it can be clearly seen that the steel counterpart surface of the PZD/rGO/MoS_2/BMI composite with 0.4 wt% PZD/rGO/MoS_2 becomes milder and has few notches. These SEM images are very consistent with the lower friction coefficient and wear rate of the 0.4 wt% PZD/rGO/MoS_2/BMI composite, suggesting that the proper amount of PZD/rGO/MoS_2 can improve the reducing-friction and wear-resistance properties of the neat BMI resin.

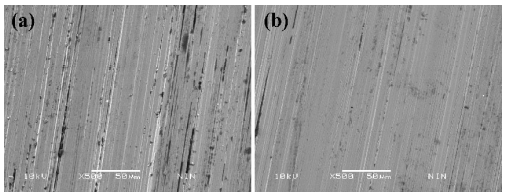

Fig. 10. SEM images of the steel counterpart surface of (a) the neat BMI, (b) 0.4 wt% PZD/rGO/MoS_2/BMI composites.

The thermal property of the neat BMI resin and the composite with 0.6 wt% PZD/rGO/MoS_2 are measured by TGA (as shown in Fig. 11). The initial thermal decomposition temperature of the neat BMI resin and the composite is approximately same and high. However, the char yield of the 0.6 wt% composite at 800 °C is 31.36%, an increase of as much as 11.36% compared to that of the neat BMI resin (28.16%), indicating that the addition of PZD/rGO/MoS_2 can improve the thermal property of the BMI resin. This excellent thermal property can protect the composites from the harm of high heat during the wear process.

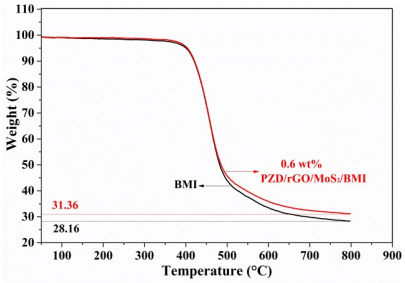

Fig. 11. TGA curves of neat BMI and 0.6 wt% PZD/rGO/MoS_2/BMI composite.

4 Conclusions

The PZD/rGO/MoS_2 hybrid nanoparticles were prepared by a one-pot noncovalent method, and then were incorporated into BMI resin as additive to fabricate PZD/rGO/MoS_2/BMI composites. The mechanical, thermal and tribological properties of the composites can be improved by suitable addition of PZD/rGO/MoS_2. When the addition amount is 0.6 wt%, the composite shows the maximum impact and flexural strength, which are increased of as much as 21.52% and 32.12% compared to those of the neat BMI resin, respectively. Furthermore, the PZD/rGO/MoS_2/BMI composite exhibits the lowest friction coefficient of about 0.06 and volume wear rate of 1.80×10^{-6} $mm^3/(N \cdot m)$ with 0.4 wt% of the PZD/rGO/MoS_2, indicating that the presence of rGO/MoS_2 hybrid nanosheets can greatly improve the reducing-friction and wear-resistance properties. This is mainly ascribed to the unique layered structure of PZD/rGO/MoS_2 hybrid nanoparticles, enhanced toughness of the composites, good interfacial adhesion and compatibility between PZD/rGO/MoS_2 and BMI matrix, as well as the synergistic effect between nanosheets of exf-MoS_2 and rGO.

Acknowledgements

This work is financially sponsored by the Seed Foundation of Innovation and Creation for Graduates Students in Northwestern Polytechnical University (Z2015028) and the PhD Programs Foundation of the Ministry of Education of China (20136102110049) and the Doctorate Foundation of Northwestern Polytechnical University (CX201429).

Notes and references

1 S. Stankovich, D. A. Dikin, G. H. B. Dommett, K. M. Kohlhaas, E. J. Zimney, E. A. Stach, R. D. Piner, S. B. T. Nguyen and R. S. Ruoff, *Nature*, 2006, **442**, 282-286.
2 N. Guo, D. Hu, H. Wang, R. Wang and Y. Xiong, *Polym. Bull.*, 2013, **70**, 3031-3040.
3 M. Liu, Y. Duan, Y. Wang and Y. Zhao, *Mater. Design*, 2014, **53**, 466–474.
4 K. K. Mahesh, F. M. B. Fernandes, R. J. C. Silva and G. Gurau, *Physics Procedia*, 2010, **10**, 22–27.
5 C. Gao, Y. Wang, D. Hu, Z. Pan and L. Xiang, *J. Nanopart. Res.*, 2013, **15**, 301-307.
6 K. S. Novoselov, A. K. Geim, S. Morozov, D. Jiang, Y. Zhang, S. Dubonos, I. Grigorieva and A. Firsov, *Science*, 2004, **306**, 666-669.
7 K. Novoselov, A. K. Geim, S. Morozov, D. Jiang, M. Katsnelson, I. Grigorieva, S. Dubonos and A. Firsov, *Nature*, 2005, **438**, 197-200.
8 A. Ferrari, J. Meyer, V. Scardaci, C. Casiraghi, M. Lazzeri, F. Mauri, S. Piscanec, D. Jiang, K. Novoselov and S. Roth, *Phys. Rev. Lett.*, 2006, **97**, 187401.
9 R. Nair, P. Blake, A. Grigorenko, K. Novoselov, T. Booth, T. Stauber, N. Peres and A. Geim, *Science*, 2008, **320**, 1308-1308.

10 K. S. Novoselov, A. K. Geim, S. V. Morozov, D. Jiang, Y. Zhang, S. V. Dubonos, I. V. Grigorieva and A. A. Firsov, *Science*, 2004, **306**, 666-669.
11 J. Wintterlin and M. L. Bocquet, *Surf. Sci.*, 2009, **603**, 1841–1852.
12 N. R. Wilson, *ACS Nano*, 2009, **3**, 2547-2556.
13 Y. Shi, *Nano Lett.*, 2012, **12**, 2784-2791.
14 Z. QZ, *J. Phys. D: Appl. Phys.*, 2011, **44**, 1-9.
15 Y. K. Yang, C. E. He, W. J. He, L. J. Yu, R. G. Peng, X. L. Xie, X. B. Wang and Y. W. Mai, *J. Nanopart. Res.*, 2011, **13**, 5571-5581.
16 H. Wang, G. Xie, Z. Zhu, Z. Ying and Y. Zeng, *Compos. Part A: Appl. Sci. Manufac.*, 2014, **67**, 268-273.
17 C. Min, P. Nie, H.-J. Song, Z. Zhang and K. Zhao, *Tribol. Int.*, 2014, **80**, 131–140.
18 K. Novoselov, D. Jiang, F. Schedin, T. Booth, V. Khotkevich, S. Morozov and A. Geim, *P. Natl. Acad. Sci. USA*, 2005, **102**, 10451-10453.
19 R. Mas-Balleste, C. Gomez-Navarro, J. Gomez-Herrero and F. Zamora, *Nanoscale*, 2011, **3**, 20-30.
20 R. Tenne, L. Margulis, M. e. a. Genut and G. Hodes, *Nature*, 1992, **360**, 444-446.
21 Y. Li, Z. Zhou, S. Zhang and Z. Chen, *J. Am. Chem. Soc.*, 2008, **130**, 16739-16744.
22 M. Osada and T. Sasaki, *J.mater.chem*, 2009, **19**, 2503-2511.
23 G. Tang, J. Zhang, C. Liu, D. Zhang, Y. Wang, H. Tang and C. Li, *Ceram. Int.*, 2014, **40**, 11575–11580.
24 X. Huang, Z. Yin, S. Wu, X. Qi, Q. He, Q. Zhang, Q. Yan, F. Boey and H. Zhang, *small*, 2011, **7**, 1876-1902.
25 S. Guo and S. Dong, *Chem. Soc. Rev.*, 2011, **40**, 2644-2672.
26 M. Xu, T. Liang, M. Shi and H. Chen, *Chem. Rev.*, 2013, **113**, 3766-3798.
27 S. Z. Butler, S. M. Hollen, L. Cao, Y. Cui, J. A. Gupta, H. R. Gutierrez, T. F. Heinz, S. S. Hong, J. Huang and A. F. Ismach, *ACS Nano*, 2013, **7**, 2898-2926.
28 J. Yao, X. Shi, W. Zhai, A. M. M. Ibrahim, Z. Xu, L. Chen, Q. Zhu, Y. Xiao, Q. Zhang and Z. Wang, *Tribol. Lett.*, 2014, **56**, 573-582.
29 J. Yao, X. Shi, W. Zhai, Z. Xu, L. Chen, Q. Zhu, Y. Xiao, Q. Zhang and Z. Wang, *Tribol. Lett.*, 2014, **56**, 573-582.
30 C. Y. Yuan, S. Y. Chen, C. H. Tsai, Y. S. Chiu and Y. W. Chen‐Yang, *Polym. Advan. Technol.*, 2005, **16**, 393-399.
31 H. R. Allcock, M. F. Welker and M. Parvez, *Cheminform*, 1992, **4**, 296-307.
32 M. Zhang, H. Yan, X. Yang and C. Liu, *RSC Adv.*, 2014, **4**, 45930-45938.
33 J. Zhu, M. Chen, H. Qu, X. Zhang, H. Wei, Z. Luo, H. A. Colorado, S. Wei and Z. Guo, *Polymer*, 2012, **53**, 5953–5964.
34 O. Y. Posudievsky, O. A. Khazieieva, V. V. Cherepanov, G. I. Dovbeshko, A. G. Shkavro, V. G. Koshechko and V. D. Pokhodenko, *J. Mater. Chem. C*, 2013, **1**, 6411-6415.
35 K. Chang and W. Chen, *ACS Nano*, 2011, **5**, 4720-4728.
36 E. Aharon, A. Albo, M. Kalina and G. L. Frey, *Adv. Funct. Mater.*, 2006, **16**, 980-986.
37 K. Chang and W. Chen, *J. Mater. Chem. A*, 2011, **21**, 17175-17184.
38 W. Wei, X. Huang, K. Chen, Y. Tao and X. Tang, *RSC Adv.*, 2012, **2**, 3765-3771.
39 A. Elass, G. Vergoten, P. Dhamelincourt and R. Becquet, *Electronic Journal of Theoretical Chemistry*, 1997, **2**, 11-23.
40 K. Zhang, H.-J. Kim, X. Shi, J.-T. Lee, J.-M. Choi, M.-S. Song and J. H. Park, *Inorg. Chem.*, 2013, **52**, 9807-9812.
41 Y. Liu, L. Jiao, Q. Wu, Y. Zhao, K. Cao, H. Liu, Y. Wang and H. Yuan, *Nanoscale*, 2013, **5**, 9562-9567.
42 S. T. K. Bindu, A. B. Nair, B. T. Abraham, P. M. S. Beegum and E. T. Thachil, *Polymer*, 2014, **55**, 3614–3627.
43 H. Yan, S. Li, Y. Jia and X. Ma, *RSC Adv.*, 2015, **5**.
44 J. Y. Wang, S. Y. Yang, Y. L. Huang, H. W. Tien, W. K. Chin and C. C. M. Ma, *J.mater.chem*, 2011, **21**, 13569-13575.
45 Q. Lin, L. Qu, Q. Lü and C. Fang, *Polymer Testing*, 2013, **32**, 330–337.
46 C. Liu, H. Yan, Z. Chen, L. Yuan and T. Liu, *J. Mater. Chem. A*, 2015, **3**, 10559-10565.
47 Y. Xu, W. Hong, H. Bai, C. Li and G. Shi, *Carbon*, 2009, **47**, 3538-3543.